



Muthu, M., Yang, E.-H. and Unluer, C. (2021) Effect of graphene oxide on the deterioration of cement pastes exposed to citric and sulfuric acids. *Cement and Concrete Composites*, 124, 104252. (doi: [10.1016/j.cemconcomp.2021.104252](https://doi.org/10.1016/j.cemconcomp.2021.104252)).

This is the Author Accepted Manuscript.

There may be differences between this version and the published version. You are advised to consult the publisher's version if you wish to cite from it.

<http://eprints.gla.ac.uk/251249/>

Deposited on: 08 September 2021

Enlighten – Research publications by members of the University of Glasgow
<http://eprints.gla.ac.uk>

1 **Effect of graphene oxide on the deterioration of cement pastes exposed to citric and**
2 **sulfuric acids**

3
4 Murugan Muthu^{a,b}, En-Hua Yang^a, Cise Unluer^{c,*}

5
6 ^a School of Civil and Environmental Engineering, Nanyang Technological University,
7 50 Nanyang Avenue, Singapore 639798, Singapore

8 ^b Larsen & Toubro Construction Research and Testing Center, Mount Poonamallee Road,
9 Manapakkam, Chennai 600089, India

10 ^c School of Engineering, University of Glasgow, G12 8LT, Glasgow, United Kingdom

11
12 * Corresponding author. E-mail address: Cise.Unluer@glasgow.ac.uk

13
14
15 **ABSTRACT**

16
17 Acid-induced deterioration reduces the service life of concrete and requires high maintenance
18 costs. This study examined the deterioration of graphene oxide (GO)-modified cement pastes
19 exposed to 1 M citric acid (C₆H₈O₇) and 1 M sulfuric acid (H₂SO₄) environments for two
20 weeks. Changes in the physical and chemical properties of the binder matrix were determined
21 by the assessment of fresh and hardened properties, and a detailed microstructural analysis
22 involving SEM-EDS, XRD, FT-IR and TGA-DTG. The formation of a thick earlandite- and
23 gypsum-like salt was observed in the altered areas of all samples after citric acid and sulfuric
24 acid attacks, respectively. A consistent reduction in the mass loss and sectional area loss was
25 recorded as the GO content increased from 0 to 0.09 wt.% under both acid environments, also
26 supported by microstructural analysis and micro-hardness results. The decline in deterioration
27 under these acid environments was associated with the increased resistance provided by GO
28 that reduced the penetration of aggressive chemical species into the matrix. Determination of
29 an optimum GO content to achieve a balance between reaction mechanisms, fresh properties
30 and durability is critical for improved performance in the long-term.

31
32 **Keywords:** Portland cement; graphene oxide; acid attack; deterioration; microstructure

33 1. INTRODUCTION

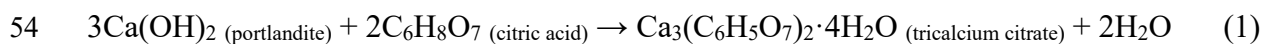
34

35 The most likely failure scenarios of concrete involve physical as well as chemical effects such
36 as acid-induced deterioration, which can reduce the service life of concrete [1], resulting in
37 high maintenance costs for critical applications (e.g. wastewater facilities) [2]. Concrete pipes
38 and other elements involved in collecting, storing, and treating wastewater are essential
39 building components used for the treatment of wastewater in sanitary, stormwater and sewer
40 environments [3]. Concrete structures operating under such acidic mediums are susceptible to
41 chemical and biogenic attacks, increasing their vulnerability to deterioration.

42

43 Wastewater generated by agricultural and agro-food industries is a mixture of silage juices,
44 liquid manure, molasses, whey, and distillery residues. The existence of either monocarboxylic
45 (acetic, propionic, lactic), dicarboxylic (succinic, oxalic, tartaric, malic) or tricarboxylic (citric)
46 acids or their combination in sewage environments regulates the pH value, which generally
47 ranges between 4 and 8 [3, 4]. These organic acids partly dissociate in water and react with the
48 binder matrix consisting of calcium silicate hydrate (C-S-H), portlandite/calcium hydroxide
49 (CH), ettringite (AFt), monosulfate (AFm) and anhydrous clinker compounds. These
50 interactions lead to the precipitation of calcium (Ca)-bearing salts, which usually dissolve in
51 the external media [5]. For instance, the reaction between portlandite and citric acid results in
52 the precipitation of tricalcium citrate salt, as shown in Equation 1.

53



55

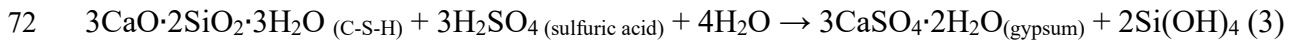
56 Another cause for the deterioration of concrete pipes is linked with the liberation of sulfuric
57 acid (H_2SO_4) in the presence of microorganisms in sanitary wastewater sources. This damage,
58 which is often referred to as "microbial induced concrete corrosion" (MICC), is commonly
59 observed in concrete pipes and results in substantial damage [1, 6, 7]. The anaerobic digestion
60 of sewage results in the liberation of hydrogen sulfide (H_2S) gas, which metabolizes with
61 oxygen by aerobic bacteria, thereby producing H_2SO_4 solution [7, 8]. During MICC, the sulfate
62 ions (SO_4^{2-}) react with the binder products (mainly CH, C-S-H, and monosulfate) and produce
63 gypsum and ettringite, as shown in Equations 2-4. The formation of these products is
64 accompanied by an increase in volume and pressure in concrete, leading to internal cracking
65 that can result in structural failure [9]. The current solutions on improving the resistance of
66 concrete pipes against chemical and biogenic attacks include the modification of concrete mix

67 using pozzolanic materials, sulfate-free aggregates, polymeric fibers, and adoption of special
68 surface treatment and curing methods [10].

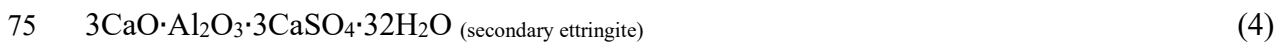
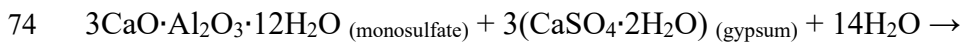
69



71



73



76

77 Advancements in nanotechnology has opened new avenues for the enhancement of the
78 mechanical properties and durability of concrete. Some of the nanomaterials popularly used in
79 cement modification include carbon nanotubes, carbon nanofibers, nano- silica, alumina, and
80 titanium dioxide [11-15]. Investigation of the performance of concrete mixes involving the use
81 of nanomaterials under acidic conditions are important for developing a comprehensive
82 understanding of the structural integrity of vulnerable structures. Under acidic conditions,
83 portlandite is prone to severe dissolution, followed by the dissolution of AFt, AFm and C-S-H
84 [16]. It has been widely reported that the effective dispersion of colloidal nano-silica in the
85 binder matrix can significantly delay concrete deterioration under acidic mediums [14, 17].
86 This improvement was associated with the enhancement of the secondary C-S-H formation and
87 reduction of the availability of portlandite in the presence of nano-silica, which was similar to
88 the effect observed via the use of pozzolanic materials (e.g. fly ash and slag) [17, 18].

89

90 The modification of cementitious mixes at nanoscale via the use of graphene and its derivatives
91 such as graphene oxide (GO) has been investigated in the context of their crack-bridging effects
92 [19, 20]. GO is an atomically thin sheet of graphite that is covalently decorated with oxygen-
93 derived functional groups, either on the basal plane or at the edges [21, 22]. The sheet-like
94 morphology, active functional groups, high surface area, and excellent mechanical properties
95 of GO ($\text{C}_x\text{O}_y\text{H}_z$) make it an ideal additive to cement mixes [23, 24]. GO can homogeneously
96 disperse in water, unlike other carbon-based materials (e.g. carbon nanotubes and carbon
97 nanofibers) [25, 26]. The economical extraction of GO from natural graphite is feasible at a
98 large scale via the Hummers' method [27, 28]. This synthesized GO has a wrinkled sheet-like
99 structure, and its basal plane and edges are grafted with oxygen-containing functional groups

100 [27]. GO typically has a high surface area of $\sim 1700 \text{ m}^2/\text{g}$ and its in-plane Young's modulus
101 ranges between 210 and 470 GPa. The thickness and lateral dimension of a single layer GO
102 sheet are typically 0.7-1 nm and 0.1-100 μm , respectively [29]. Previous studies reported the
103 use of GO at a content of 0.02-0.08 wt.% to improve the mechanical performance of cement-
104 based mixes [30-32]. Increasing the content beyond these values could result in the
105 agglomeration of the GO flakes, thereby reducing performance [25].

106
107 While the effects of GO dosage on the workability, rheology, shrinkage, electrical resistivity,
108 microstructure, mechanical strengths, and permeability of cementitious composites have been
109 studied [24, 33-37], the performance and microstructural changes in GO-modified cement
110 composites exposed to aggressive aqueous mediums (e.g. wastewater, sea water and ground
111 water) has not been fully investigated. Aiming to fill this gap in the literature, this study
112 examined the deterioration mechanisms of cement mixes containing 0-0.09 wt.% GO under
113 citric and sulfuric acids, which simulated the chemical attack often occurring in essential
114 infrastructure operating in sewers and wastewater treatment plants. The primary goals of this
115 study were to (i) understand the alteration process of GO-modified cement pastes exposed to
116 citric and sulfuric acids and (ii) reveal the influence of different GO contents on the chemical
117 resistance of cement mixes.

118
119 To validate the relative degree of deterioration, the loss in specimen mass and sectional area
120 were recorded and compared at the end of each acid attack exposure. The chemical,
121 mineralogical and mechanical changes in the prepared paste specimens due to calcium leaching
122 were assessed using scanning electron microscopy (SEM), in conjunction with energy
123 dispersive spectroscopy (EDS), thermogravimetric analysis (TGA-DTG), X-ray diffraction
124 (XRD), Fourier transform infrared spectroscopy (FT-IR), and Vickers micro-hardness
125 analyses. The changes in the pH and conductivity of the two acidic solutions were also
126 continuously recorded. The obtained results led to a discussion on the effects of the
127 characteristics and content of GO on the rheology and hydration of cement mixes. Overall, the
128 findings of this project could enable the development of ideal cement mixes with increased
129 durability under acidic environments.

130 131 132 **2. EXPERIMENTAL PROGRAM**

133

134 2.1. Materials

135

136 The main binder used in sample preparation was CEM I 52.5 N Portland cement (PC) obtained
137 from EnGro Corporation Ltd. (Singapore) [38]. The chemical composition of this PC is shown
138 in Table 1. The water-soluble GO used in this study was procured from Sigma Aldrich Ltd.
139 (Singapore). It was extracted from 99% carbon-based natural graphite with an average size of
140 150 μm by using a modified Hummers' method, as reported in Li et al. [27]. According to the
141 information provided by the manufacturer, this monolayer GO could disperse in any polar
142 solvents and had an oxygen content exceeding 36 wt.%. In addition to GO, a polycarboxylate
143 (PCE)-based superplasticizer with a solid content of 35 wt.% was used to prepare the GO-
144 modified cement pastes.

145

146 **Table 1** Chemical composition (wt.%) of PC used in this study.

147

CaO	SiO ₂	Al ₂ O ₃	Fe ₂ O ₃	MgO	SO ₃	Na ₂ O	K ₂ O	Ignition loss
63.6	22.7	5.6	2.9	1.4	1.5	0.3	0.4	1.6

148

149 GO was characterized via X-ray photoelectron spectroscopy (XPS, Kratos Analytical Axis
150 Supra), FT-IR (Thermo Scientific Nicolet iS50), SEM-EDS (JEOL JSM-7600F) and XRD
151 (Bruker D8 Advance). Before the XPS scan, GO was dried overnight at 80°C, washed with
152 acetone, deposited on a filter paper and vacuum desiccated for 7 days. It was then pressed onto
153 an indium wrapped carbon substrate and mounted into the XPS machine, operating with a
154 monochromated aluminum K α source (~1486.6 eV). For the reproducibility of data, the XPS
155 scan was repeated 3 times by following a similar spot size, dwell time, and resolution of 400
156 μm , 0.05 seconds, and 0.1 eV, respectively. The dry GO flake was directly placed under the
157 metal tip of the FT-IR machine and scanned for a wavelength range of 4000-400 cm^{-1} . To
158 conduct the XRD scan, dried GO was powdered to a size smaller than 54 μm by using a mortar
159 and pestle, and tested at a range of 5-80° 2 θ and a scanning rate of 0.02° 2 θ per minute. The dry
160 GO flake was also fixed onto a steel stub using a carbon tape and imaged using SEM operated
161 at a voltage of 5-15 kV.

162

163

164 2.2. Sample preparation

165

166 Seven cement paste mixes, with different GO contents of 0% (GO-0), 0.015% (GO-1), 0.03%
167 (GO-2), 0.045% (GO-3), 0.06% (GO-4), 0.075% (GO-5) and 0.09% (GO-6) were prepared in
168 this study. While higher GO dosages can demand higher PCE contents, all mixes presented in
169 this study involved a constant PCE content of 0.1 wt.% and a water/cement (w/c) ratio of 0.35
170 to avoid delays in setting time, maintain uniformity in sample preparation and avoid variation
171 amongst different samples. To avoid the agglomeration of GO, the solution mixture containing
172 GO, PCE, and water was sonicated for 20 minutes before being used in the preparation of
173 cement mixes. The prepared mix was cast in $15 \times 15 \times 50$ mm³ prismatic acrylic moulds and
174 consolidated by using a vibration table. All samples were demolded after 24 hours and cured
175 under water for up to two weeks as cement-based samples gain a majority of their ultimate
176 strength within 14 days of curing.

177

178

179 **2.3. Calorimeter and rheometer tests**

180

181 The heat flow due to the hydration of GO-modified cement pastes was studied at 30°C by using
182 a Calmetrix I-Cal 8000 HPC calorimeter, in line with ASTM C1702 [39]. To record the heat
183 of hydration for up to 24 hours, the fresh pastes were immediately loaded into the calorimeter
184 channels within a few seconds of mixing.

185

186 The rheological properties (e.g. shear stress and apparent viscosity) of GO-modified cement
187 pastes were also tested under ambient conditions by using a HAAKE Mars III rheometer. The
188 sample measuring cell was fixed with a titanium (Ti)-based top plate and fitted with a sensor
189 and a 20 mm diameter proliferated base plate. A spoon filled with fresh cement paste was
190 placed on this cell fixture and pressed against the base plate with a load of 0.5 N. The excess
191 cement paste was removed and the top plate was rotated at a speed of 50 rotations/minute for
192 30 seconds. After this pre-shearing process, the shear rate was increased from 1 to 100 s⁻¹
193 within 100 seconds to study the stress growth pattern for a total duration of 130 seconds.

194

195

196 **2.4. Acid attack**

197

198 Laboratory reagents 95% concentrated sulfuric acid solution (H_2SO_4) and 99% pure citric acid
199 powder ($\text{C}_6\text{H}_8\text{O}_7$) procured from Sigma Aldrich Ltd. (Singapore) were used in this study. Acid
200 attack on the prepared cement pastes was conducted by immersing the cured samples in a 150
201 mL glass beaker containing 1 M acidic solution for two weeks. These relatively high acid
202 concentrations were used to facilitate the generation of data in a short time by accelerating the
203 deterioration process. Acid exposure took place under ambient conditions (i.e. 25°C and 65%
204 RH). Both the $\text{C}_6\text{H}_8\text{O}_7$ and H_2SO_4 solutions were replenished on a weekly basis during the
205 testing period to ensure the samples were constantly exposed.

206

207

208 **2.4.1. Sample mass and sectional area**

209

210 The prepared samples were immersed in $\text{C}_6\text{H}_8\text{O}_7$ and H_2SO_4 solutions for up to two weeks. The
211 mass of each sample was recorded at the end of acid exposure by using a 0.001 g precision
212 balance. Before mass measurements, each sample was washed using a water jet and wiped with
213 a dry tissue paper. Washing was done to remove the loose Ca-bearing salts on the sample
214 surfaces. Subsequently, the exposed samples were sectioned into multiple pieces by using a
215 diamond-tipped precision saw to reveal the zone altered by citric and sulfuric acids. The
216 boundary of the altered zone was located and analyzed with a Optem Zoom 70XL stereo
217 microscope using high magnification lenses. The deteriorated region revealed a different
218 colour, unlike the unaltered core material (i.e. sound zone). The boundaries of the altered zone
219 were identified and the area of discolouration observed in the image was measured by using an
220 imaging software (Image-Pro Premier, Version 9.1, Media Cybernetics, United States). Four
221 cut-sections from each sample were analyzed via this procedure and the average sectional area
222 loss was calculated by dividing the deteriorated area by the original cross-sectional area of the
223 sample.

224

225

226 **2.4.2. Solution pH and conductivity**

227

228 The prepared samples were immersed in $\text{C}_6\text{H}_8\text{O}_7$ and H_2SO_4 solutions for up to two weeks,
229 during which the change in the pH and conductivity of the acid solutions were periodically
230 recorded by using a Horiba F-52 pH meter and ThermoScientific Orion Star A212 conductivity
231 meter, respectively. Before the measurements, the pH meter was 3-point calibrated, whereas

232 the conductivity meter was 2-point calibrated at 25°C by using the National Institute of
233 Standards and Technology (NIST) certified buffer solutions. The average of three
234 measurements was taken for each data point.

235

236

237 **2.4.3. SEM-EDS and micro-hardness**

238

239 The cut-sections (i.e. before and after acid exposure) were dried under vacuum for 48 hours at
240 30°C, epoxy impregnated by using a Buehler Cast-Vac-220 vacuum impregnation machine and
241 left undisturbed for 8 hours. The hardened epoxy polymer was then demolded and polished
242 with a Buehler MetaServ 250 grinder-polisher, following the procedure outlined in an earlier
243 study [40]. These polished sections were characterized by SEM-EDS operating under the
244 backscattered electron (BSE) imaging mode. The dry polished samples were mounted onto
245 steel stubs by using a carbon adhesive before they were analyzed under SEM.

246

247 The prepared samples were also analysed by a Wilson Tukon-1202 Vickers hardness tester, in
248 compliance with ASTM E384 [41]. A load (P) of 0.3 kilogram-force (kgf) with a loading time
249 of 10 seconds was adopted to create an indent in the polished sample. Multiple indents were
250 made on each sample before and after exposure to C₆H₈O₇ and H₂SO₄ solutions. Indentations
251 were meticulously chosen by using optical micrographs and analyzing the data to select the
252 micro-indentations that represented the binder matrix. Two opposite diagonal lengths (d₁ and d₂) of
253 each indent mark were recorded by using the optical microscope within the hardness tester.
254 The area of indentation was determined by multiplying these two diagonal lengths. The Vickers
255 hardness number (HV) was calculated by dividing 1.854xP (in kgf) with the area of indentation
256 (in mm²) [42].

257

258

259 **2.4.4. TGA-DTG, XRD and FT-IR**

260

261 The soft altered zone of the binder matrix was sampled by carefully scratching this area, during
262 which care was taken to avoid the intermixing of altered and unaltered zones. The collected
263 samples were vacuum dried for 48 hours at 30°C, ground to a size smaller than 54 µm by using
264 a mortar and pestle, and analyzed under TGA-DTG, XRD and FT-IR. For TGA-DTG,
265 performed with a Perkin Elmer TGA 4000, the samples were heated from 35°C to 900°C at a

266 rate of 10°C per minute under a nitrogen flow. The XRD scan was done by a Bruker D8
267 Advance, using Cu K α radiation (40 kV, 30 mA) at a scanning rate of 0.02° 2 θ per minute,
268 within a scan range of 5-80° 2 θ . FT-IR scan was conducted at a wavelength range of 4000-400
269 cm⁻¹ by using a Thermo Scientific Nicolet iS50 Model instrument.

270

271

272 **3. RESULTS AND DISCUSSION**

273

274 **3.1. Characterization of GO**

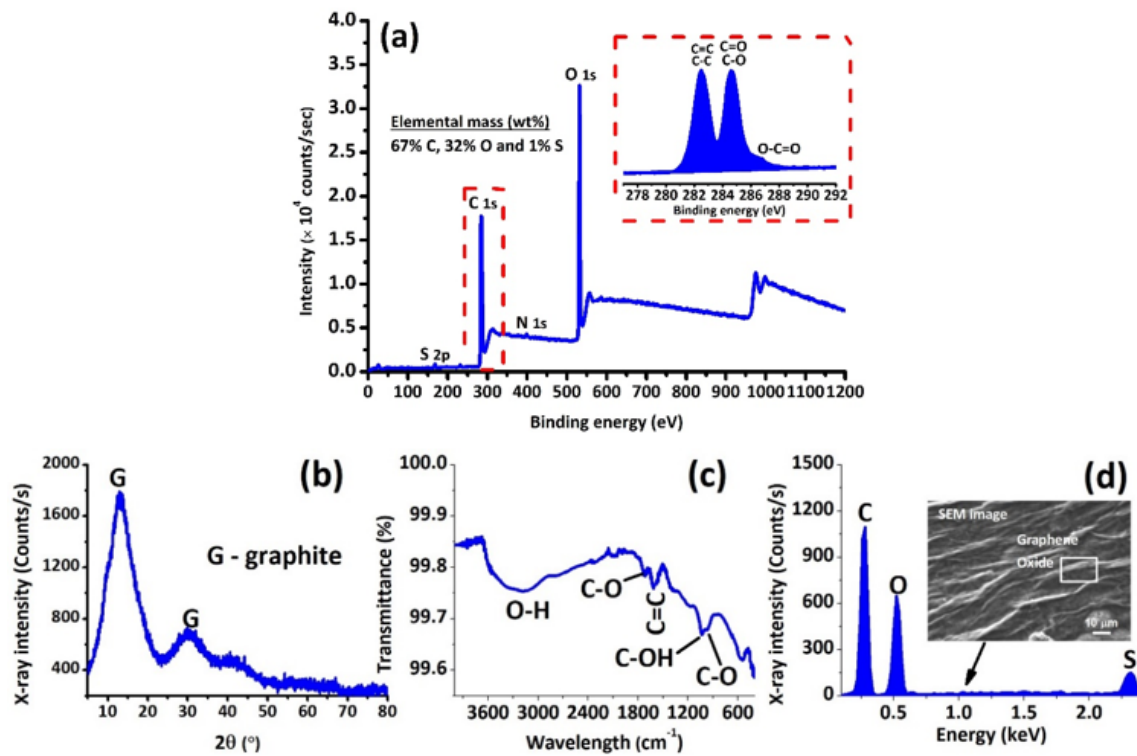
275

276 The GO synthesized using Hummers' method is functionalized with epoxy, hydroxyl, carbonyl,
277 and carboxyl groups. These oxygen-containing functional groups are covalently bonded to the
278 edges and basal plane of graphene sheets [29]. The functionalization degree was analyzed by
279 XPS, whose results are shown in Fig. 1(a). The obtained XPS spectra was used to quantify the
280 mass concentration of elements forming the GO material, which contained carbon (65.9 wt.%),
281 oxygen (32.1 wt.%), sulfur (1.4 wt.%), and nitrogen (0.6 wt.%). In general, sulfur and nitrogen
282 traces are often found in GO solutions synthesized by using the Hummers' method [27]. The
283 concentrations of sulfur and nitrogen in the GO used in this study were marginal and within
284 the limits suggested by previous studies [29, 43].

285

286 Further characterization of GO via XRD (Fig. 1(b)), FT-IR (Fig. 1(c)), and SEM-EDS (Fig.
287 1(d)) revealed information on its composition and microstructure, which consisted of twisted
288 flakes with a wrinkled surface structure on (Fig. 1(d)). The oxygen-to-carbon ratio by mass
289 was about 0.5, confirming that GO was highly oxygenated and hydrophilic. The carbon (C1s)
290 spectrum, processed from the XPS spectra to establish the chemical states of carbon within
291 GO, revealed three major peaks at binding energies of 282.4 eV, 284.6 eV, and 286.5 eV. These
292 peaks correlated with the existence of three carbon states in GO: (i) graphitic carbon (sp² and
293 sp³ hybridized), (ii) carbonyl (C=O and C-O) and (iii) carboxyl (COOH) structures, which was
294 in line with the findings of previous studies [29, 43]. The XRD pattern (Fig. 1(b)) revealed two
295 main peaks at 13.1° and 30.5° 2 θ , indicating the existence of a graphite-like structure in the
296 powdered GO. Similarly, the FT-IR bands (Fig. 1(c)) at 1735 cm⁻¹, 1210 cm⁻¹, and 1050 cm⁻¹
297 were associated with the presence of carbonyl (C=O), ether (C-O-C), and hydroxyl (C-OH)
298 functional groups in GO.

299



300
301
302 **Fig. 1** Characterization of GO, showing its: (a) XPS spectra (inset picture showing its C1s
303 pattern), (b) XRD pattern, (c) FT-IR spectra and (d) SEM-EDS results

304
305
306 **3.2. Effect of GO dosage on the cement hydration and rheological properties**

307
308 Fig. 2 shows the calorimetry results of GO-modified cement pastes during the first 24 hours of
309 hydration. When compared to the control sample (GO-0), GO-1 and GO-2 samples revealed
310 an increase in their initial rate of heat evolution. A different scenario was observed in the
311 remaining samples with higher GO contents (GO-3, GO-4, GO-5, and GO-6), which
312 demonstrated similar or lower heat evolution patterns than the control sample. The negatively
313 charged GO sheets electrostatically interact with the calcium ions that dissolve from the
314 tricalcium silicate and tricalcium aluminate and behave as nucleation seeds (i.e. accelerating
315 the hydration process) [32, 37, 44, 45]. Increasing the GO dosage beyond 0.03 wt.% may result
316 in their absorbing onto the surfaces of cement particles, thereby limiting the dissolution of
317 calcium aluminates and retarding hydration [24, 40]. These results indicate the significance of
318 GO content in improving the reaction kinetics of PC mixes.

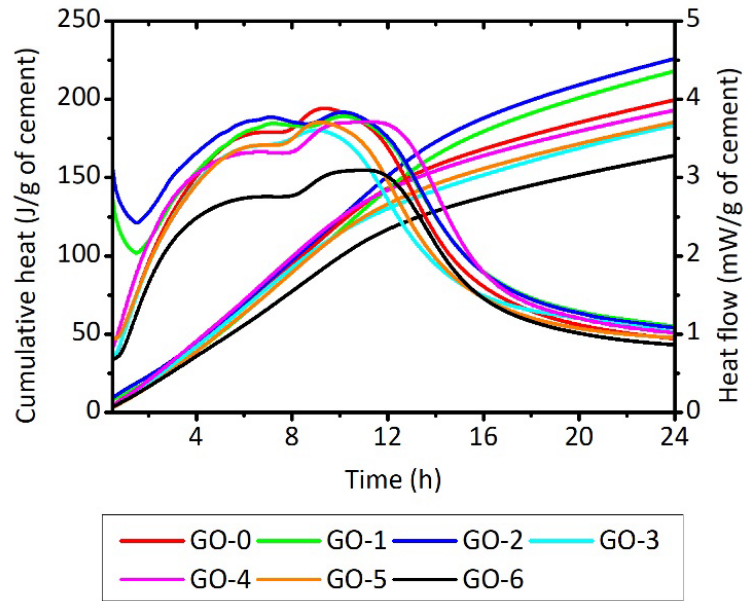


Fig. 2 Calorimetry results presenting the cumulative heat and heat flow curves of all GO-modified cement samples

Fig. 3(a) shows the flow curve pattern of GO-modified cement pastes analysed under an increasing shear rate of 1-100 s^{-1} , revealing the shear-thinning behaviour of the fresh pastes. The Herschel-Bulkley rheological prediction model, as shown in Equation 5 (i.e. where τ is the shear stress (Pa), τ_0 is the yield shear stress (Pa), γ is the shear rate (s^{-1}), and K is consistency (Pa.sⁿ)), was reported to fit the experimental rheometer data of samples containing 0.03, 0.05, and 0.1 wt.% GO better than modified Bingham, Herschel-Bulkley, Bingham, and Casson models [33]. Previous studies [46] examined the rheological properties of oil well cement slurries modified with carbon nanofiber and graphene nanoplatelets, which showed typical shear-thinning behaviour with decreased viscosity at high shear rates (i.e. up to 1000 s^{-1}). The Vom Berg (VB) rheological model, given in Equation 6 (i.e. where n is a power rate index, and b and c are material constants) fitted the experimental data of these GO-modified cement slurries better than the Bingham, Herschel-Bulkley, and Vocadlo rheological models. The VB model uses an inverse hyperbolic function (\sinh^{-1}), whereas the Herschel-Bulkley model is assisted by an exponential function. In this study, the cement pastes with and without GO sheets exhibited a Herschel-Bulkley fluid, which demanded minimum shear stress for initial flow, demonstrating smaller increments in stress with increasing shear rate.

$$\tau = \tau_0 + K(\gamma)^n \text{ (Herschel-Bulkley model)} \quad (5)$$

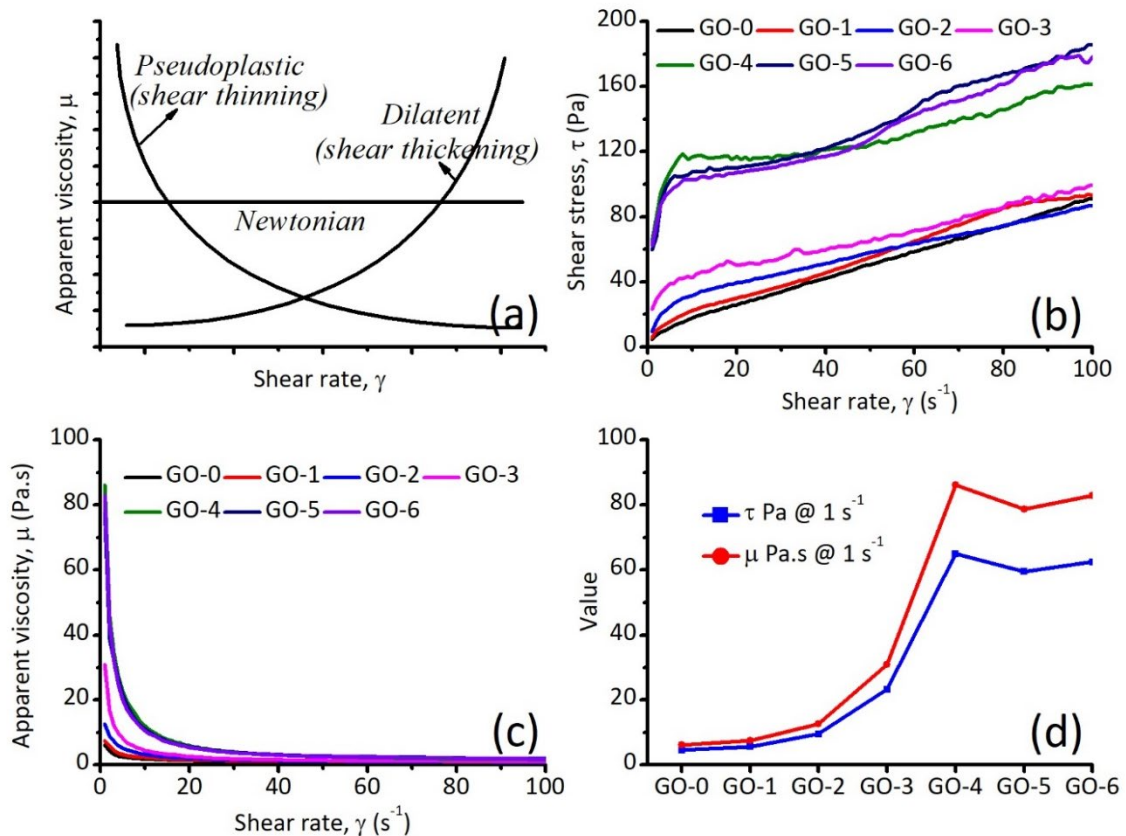
343

344 $\tau = \tau_0 + b \cdot \sinh^{-1}(\gamma/c)$ (Vom Berg model) (6)

345

346 In this study, the apparent viscosity (μ) of all fresh GO-modified cement pastes declined with
347 increasing shear rate. This could explain the progressive separation of GO sheets and cement
348 particles after mixing and their alignment in the direction of flow. Using the τ and μ values at
349 the initial shear rate of 1 s^{-1} to validate flow, the initial viscosity (at 1 s^{-1}) of GO-0, GO-1, GO-
350 2, GO-3, GO-4, GO-5, and GO-6 samples was found to be 6.1, 7.5, 12.6, 30.91, 86.2, 78.7, and
351 82.8 Pa·s, respectively. The μ of cement pastes increased with increasing GO content from 0
352 to up to 0.06 wt.%, followed by a slight decrease beyond this limit. This trend was an indication
353 of the role of GO content in controlling the flow of cement pastes. The notable change in the
354 initial τ from GO-3 to GO-4 could reveal the formation of flocculated structures due to the
355 agglomeration of GO and cement particles [33, 40]. The absorption of free water onto the GO
356 surfaces rather than the cement particles due to the higher GO contents of GO-4, GO-5 and
357 GO-6 samples could reduce the fluidity of these pastes, which is generally controlled by the
358 thickness of the water film surrounding the cement particles.

359



360

361

362 **Fig. 3** Rheological properties of GO-modified cement samples, showing: (a) Common flow
363 behaviour of Newtonian and non-Newtonian fluids [47], (b) shear stress curve, (c) apparent
364 viscosity curve, and (d) initial τ and μ values at a $\dot{\gamma}$ of 1 s^{-1}

365
366 The combination of calorimetry and rheological findings indicated the obvious role GO content
367 played in the reaction (i.e. hydration) mechanisms and fresh properties of cement pastes, which
368 generally reduced with increasing GO dosage. This could be mainly due to the increased
369 adsorption of free water onto the surface of GO instead of the cement particles during early
370 ages. Accordingly, limiting the GO content in the binder matrix could avoid any potential
371 hydration retardation or workability issues.

372
373

374 **3.3. Visual inspection of samples before and after acid exposure**

375

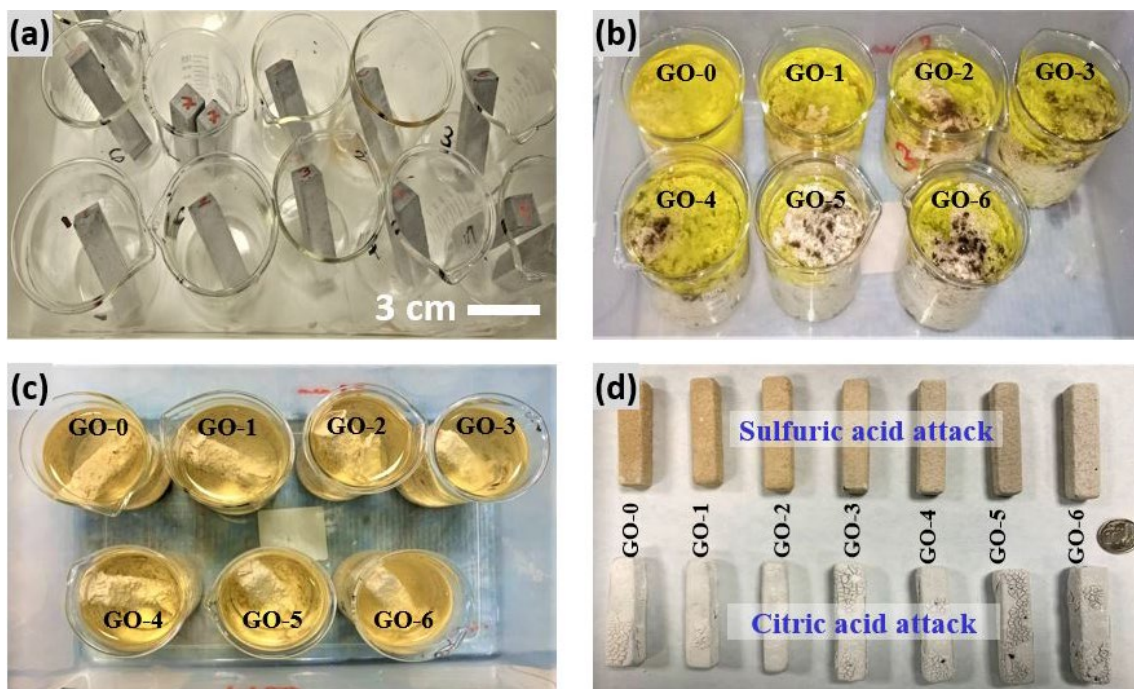
376 Acid attack on cement pastes is generally associated with the precipitation of the altered zone
377 surrounding the sound zone [48]. In this study, due to the frequent replenishment of $\text{C}_6\text{H}_8\text{O}_7$
378 and H_2SO_4 solutions, the degree of alteration of the binder matrices of the GO-modified cement
379 samples increased with exposure time. Fig. 4 shows the change in all samples before and after
380 acid attack. Initial observations revealed the more aggressive nature of the $\text{C}_6\text{H}_8\text{O}_7$
381 environment, resulting in a significant amount of leaching and nearly the total dissolution of
382 the altered zone. Two types of Ca-based salts with different solubilities form as a result of
383 $\text{C}_6\text{H}_8\text{O}_7$ and H_2SO_4 attack on the binder matrix [3, 5]. The mineralogy of these Ca-based salts
384 was controlled by the properties of binder matrix (i.e. stability of the cement hydrates and
385 porosity) and external solution (i.e. pH, k , and pKa values) [49]. Furthermore, the solubility,
386 molar volume and crystallographic structure of the sparingly soluble Ca-bearing salt also
387 influenced its properties. Alternatively, the soluble Ca-based salt, which was naturally removed
388 from the specimen surface, deposited at the bottom of the glass beaker, which was more
389 pronounced in the case of H_2SO_4 attack. The Ca-based salt that precipitated in vast quantities
390 on the sample surfaces did not have any protective effect on the remaining binder matrix.

391

392 After two weeks of exposure, a significant volume of the GO-modified cement samples were
393 altered under $\text{C}_6\text{H}_8\text{O}_7$ and H_2SO_4 exposure. In addition to the soluble Ca-bearing salts, the
394 leaching of GO sheets was also spotted in the $\text{C}_6\text{H}_8\text{O}_7$ solution (Fig. 4(b)), while this effect was
395 not visible under H_2SO_4 exposure (Fig. 4(c)). The loose Ca-based salt sticking on to the

396 surfaces of acid exposed samples was removed by using a water jet. After washing, the
 397 resulting sample (i.e. the sound zone encompassed by the altered area), as shown in Fig. 4(d),
 398 was examined to understand the deterioration processes within each sample. Samples altered
 399 by $C_6H_8O_7$ exposure appeared to be white in colour with several surface cracks, whereas
 400 samples exposed to H_2SO_4 were light yellow in colour. Previous studies Huber et al. [1], Bertron
 401 et al. [3] that inspected the degraded zone of cement samples altered by $C_6H_8O_7$ and H_2SO_4
 402 solutions reported the white and yellowish coloured products precipitated in the altered zones
 403 as calcium citrate tetrahydrate and calcium sulfate salts, respectively.

404



405

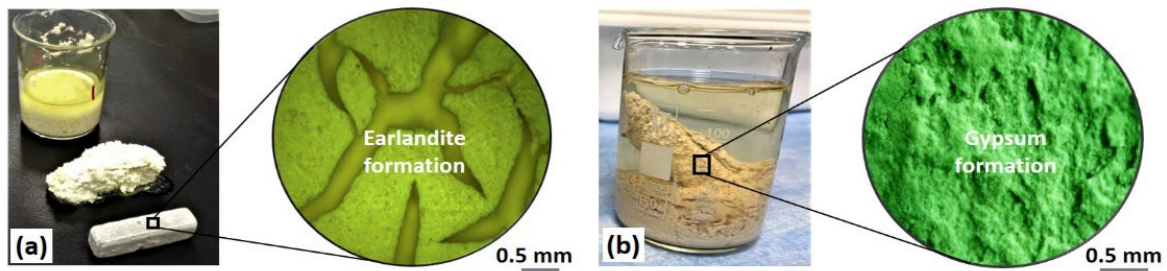
406

407 **Fig. 4** GO-modified cement samples investigated (a) before acid attack, (b) during citric acid
 408 exposure (at 14 days), (c) during sulfuric acid exposure (at 14 days) and (d) after washing
 409 following 14 days of acid exposure

410

411 Further assessment of each sample was performed with optical microscopy, which revealed the
 412 formation of micro-cracks and mineralogical changes in the binder matrix exposed to the two
 413 different acid environments (Fig. 5). A network of fine cracks was noted on the surface of the
 414 $C_6H_8O_7$ exposed samples, irrespective of the GO dosage. On the other hand, this crazing was
 415 not observed in the surfaces of samples subjected to H_2SO_4 attack. These surface cracks,
 416 generally observed during the self-desiccation of C-S-H gel in the altered zones of the binder
 417 matrix [50], could be attributed to chemical shrinkage. Accordingly, the leaching of Ca^{2+} ions

418 could produce a gradient in the calcium-to-silica ratio in the matrix, such that the driving force
419 for such shrinkage was maximum at the exterior surfaces of the samples altered by the two
420 acids. This decalcification induced shrinkage could generate differential stresses, placing the
421 exterior surfaces of samples in tension [51]. When this tensile stress reaches a level that causes
422 fracture, shallow cracks at the microscale level may form at the outer surface of the samples.
423



424
425

426 **Fig. 5** Closer view of the GO-0 sample after 14 days of exposure to: (a) citric acid and (b)
427 sulfuric acid

428
429

430 3.4. Changes in solution pH and conductivity

431

432 The test specimens were cured under tap water for two weeks followed by their immersion into
433 1 M H_2SO_4 and 1 M $C_6H_8O_7$ solutions for a further two weeks, during which the pH and
434 solution conductivity (k) were recorded, providing useful information regarding the
435 mineralization of salts over time. Fig. 6 shows the changes in pH and k values due to the
436 leaching of Ca^{2+} ions from the GO-modified samples after 14 days of exposure to tap water,
437 citric acid, and sulfuric acid. An increase in both the pH and k values was observed after water
438 curing (Fig. 6(a)), which was associated with the leaching of alkalis (Na_2O and K_2O),
439 portlandite ($Ca(OH)_2$), and free lime (CaO) from the binder matrix into the curing water.
440 Amongst all samples, GO-6 revealed the lowest increase in pH and k , which could be due to
441 the limited dissolution of portlandite and free lime from the binder matrix in the presence of
442 increased GO contents. This outcome was in line with the findings of the previous study [52],
443 which reported that the inclusion of GO significantly decreased the formation of capillary pores
444 (i.e. sizes ranging from 10 nm to 10 μm) in cement composites, which subsequently reduced
445 the leaching of Ca^{2+} and Al^{3+} ions from the matrix exposed to deionized water. Similarly, the
446 use of graphite nanoplatelets (0.05 vol.%) along with polyvinyl alcohol (PVA) fibers (3.2

447 vol.%) in industrial scale concrete pipes exposed to H₂SO₄ attack for 90 days was shown to
448 reduce water sorptivity by up to 37%, in comparison to the plain PVA-modified concrete pipes
449 (i.e. without any graphite) [53]. The inclusion of graphite in these samples reduced the growth
450 of micro-cracks and hindered the sorption of moisture from the H₂SO₄ environment. A further
451 reduction in water sorptivity by up to 50% was achieved when oxidised graphite was used
452 instead of ordinary graphite (i.e. whose surface was not treated using polymeric surfactants)
453 [54]. The modification of graphite surfaces using polyelectrolytes improved their dispersibility
454 in the cement matrix, which enhanced the service life of concrete in aggressive environments.

455

456 The initial pH (and *k*-value) of C₆H₈O₇ and H₂SO₄ solutions used in this study were 1.87 and
457 0.44 (and 7.7 and 391 mS/cm), respectively. The strength of an acid is related to its dissociation
458 constant (pK_a). The pK_{a2} (i.e. the dissociation constant for the second ionization of the acid)
459 of citric and sulfuric acids is 4.76 and 1.99 at 25°C [5]. The pH results revealed that the rate of
460 strength loss due to the leaching of calcium from the pastes was relatively fast in the C₆H₈O₇
461 solution when compared to the H₂SO₄ solution. Alternatively, the decline in the *k*-value of the
462 H₂SO₄ solution due to calcium leaching was found to be substantial, suggesting that the entry
463 of the H⁺ and SO₄²⁻ ions into the binder matrix was followed by the severe decalcification and
464 reprecipitation of the calcium-based salts in the external solution.

465

466 The rise in pH (and *k*-value) of the C₆H₈O₇ solution due to the decalcification of phases in GO-
467 0 and GO-6 samples was noted as 48% and 41% (and 3% and 9%), respectively. In contrast,
468 the rise in pH (and decline in *k*-value) of the H₂SO₄ solution due to the leaching of Ca²⁺ ions
469 from GO-0 and GO-6 samples was 102% and 70% (and 32% and 3%), respectively. Regardless
470 of their extent, these changes in the pH and *k* values of C₆H₈O₇ and H₂SO₄ solutions due to
471 calcium leaching from the binder matrices decreased with increasing GO dosage. This was a
472 clear indication of the role that GO inclusion played in slowing down the decalcification rate
473 of key phases (e.g. C-S-H, CH, AFt, AFm, and anhydrous phases) from cement pastes exposed
474 to acidic solutions.

475

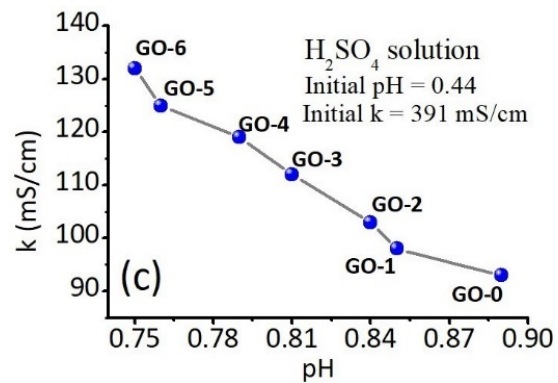
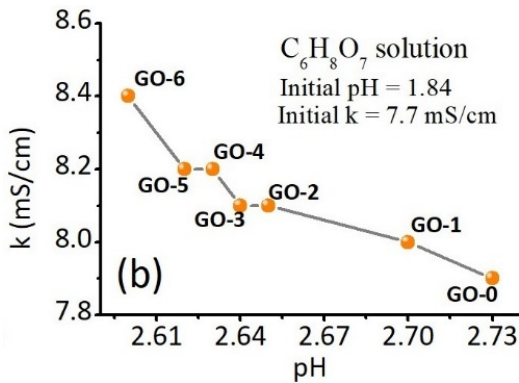
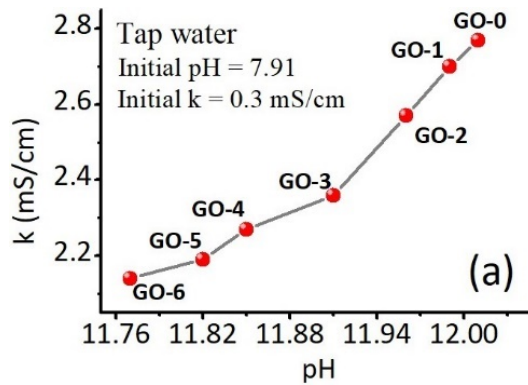


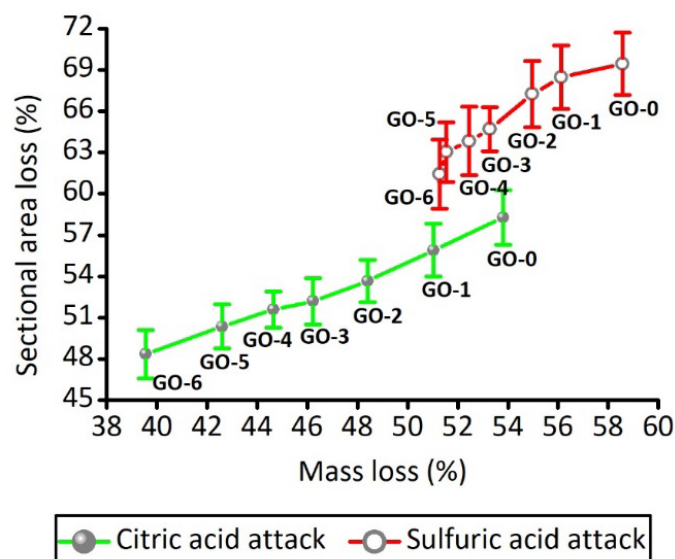
Fig. 6 Change in pH and k values due to the leaching of GO and cement hydrates from the sample matrix during exposure to: (a) tap water, (b) citric acid and (c) sulfuric acid

3.5. Loss in specimen mass and sectional area

Fig. 7 shows the mass loss and sectional area loss in GO-modified cement samples after 14 days of acid exposure. While both acidic environments led to a decline in the mass and sectional areas of all samples, the type of acid influenced the degree of calcium leaching from the binder matrix. The average mass (and sectional area) loss in GO-0 sample exposed to citric and sulfuric acids for two weeks were measured as 54% and 59% (and 58% and 69%), respectively. Alternatively, the mass (and sectional area) loss in GO-6 sample under citric and sulfuric acids were 40% and 51% (and 48% and 61%), respectively. The average depth of the degraded zone in GO-0, GO-1, GO-2, GO-3, GO-4, GO-5 and GO-6 samples after exposure to citric and sulfuric acids for two weeks was recorded as 2.66, 2.57, 2.47, 2.39, 2.28, 2.22 and 2.13 mm (under $C_6H_8O_7$); and 3.36, 3.34, 3.09, 3.05, 2.94, 2.92 and 2.85 mm (under H_2SO_4), respectively.

497 Accordingly, all measurements revealed that the degree of deterioration of the binder matrix
 498 under these two acid environments decreased with increasing GO content. The increased
 499 resistance of GO-modified samples was linked with the incorporation of GO into the binder
 500 matrix, which created a filler effect, thereby inhibiting the penetration of aggressive ions from
 501 the surrounding environment. It has been reported that the inclusion of 0.03 wt.% GO in cement
 502 pastes reduced the amount of capillary pores by up to 28%, enhancing the compressive and
 503 tensile strengths of these samples by 46% and 50%, respectively [55]. Furthermore, the use of
 504 GO increased the formation of portlandite by up to 6%, in comparison to the control sample
 505 (i.e. without any GO), which could also contribute to the improvement in performance [55].
 506

507 In line with the mechanisms suggested in previous relevant studies [56], the reinforcement
 508 effect of GO sheets on the binder matrix could be attributed to three primary reasons: (i) the
 509 high surface area of GO promotes the hydration of cement, thereby regulating the
 510 microstructure of cement hydrates; (ii) the filler effect of GO that can seal the defective regions
 511 in the binder matrix, thus densifying the microstructure; and (iii) the strong interaction between
 512 the reinforcing GO sheet and C-S-H due to chemical bonding. While these reinforcing benefits
 513 of GO were also observed in this study for GO contents of up to 0.09%, the adverse effects of
 514 increasing GO usage beyond 0.03 wt.% in the workability and hydration of fresh cement pastes
 515 were also revealed. Therefore, an intermediate GO content that could not only reduce the
 516 deterioration of cement samples against aggressive environments, but also enable the
 517 maintenance of a desired workability and hydration rate should be determined for optimum
 518 performance.
 519



521

522 **Fig. 7** Mass and sectional area losses in GO-modified cement samples after 14 days of
523 $C_6H_8O_7$ and H_2SO_4 exposure

524

525

526 **3.6. Microstructural analysis**

527

528 **3.6.1. SEM-EDS**

529

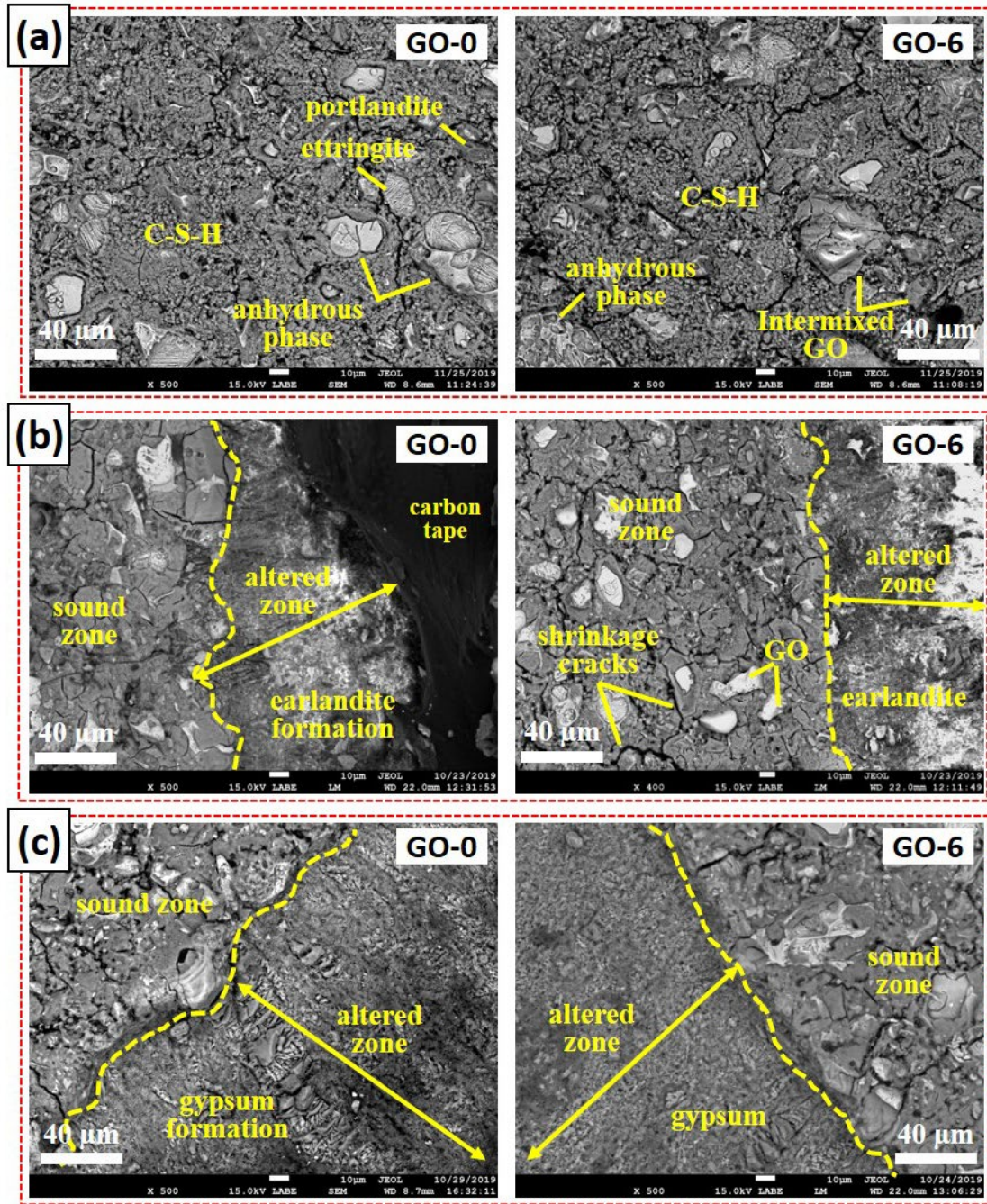
530 Fig. 8 shows the BSE images of polished surfaces of GO-0 and GO-6 samples before and after
531 acid attack (i.e. comprising both the altered and sound zones). The voids, defects and different
532 hydrate phases (C-S-H, CH, Aft, and anhydrous phases) were observed in the binder matrices
533 of both samples. These individual components could be classified via their morphology, grey-
534 scale value and chemical composition. Amongst these, the GO and cement particles seemed to
535 have an angular shape, which could be differentiated via their distinct grey-scale values (Fig.
536 8(a)). Micro-cracks were seen in these two samples before acid attack, which could have
537 formed during the drying and polishing processes. The inclusion of GO in the binder matrix
538 could have also promoted the excessive formation of autogenous shrinkage-induced micro-
539 cracks during the early ages, associated with the increased formation of C-S-H gel in the
540 presence of GO [57].

541

542 The morphologies of the altered zones of GO-0 and GO-6 samples exposed to $C_6H_8O_7$ and
543 H_2SO_4 environments were revealed in Figs. 8(b) and (c). The zone affected by the two acids
544 had a denser structure in comparison to the sound zone, which was also accompanied by the
545 formation of cracks in both samples. These cracks could have primarily formed because of
546 chemical shrinkage caused by the decalcification of the reaction products. The positioning of
547 these cracks, which ran through C-S-H while surrounding the vicinity of the cement particles
548 (Fig. 8(b), GO-6), could be an indication of the higher vulnerability of C-S-H gel to
549 decalcification induced shrinkage. While the inclusion of GO did not seem to have a significant
550 effect on the mineralogy of Ca-based salts that precipitated in the altered zone, its presence
551 inhibited the mass transfer and ionic movements between the binder matrix and the external
552 solution.

553

554 Fig. 9 shows the results of the EDS analyses conducted on GO-0 and GO-6 samples (in the
555 sound zone) before and after the acid attack. This plot, which established a link between two
556 different atomic ratios (i.e. silica-to-calcium (Si/Ca) and aluminium-to-calcium (Al/Ca)),
557 indicated the regions corresponding to C-S-H, portlandite, ettringite and monosulfate
558 formation. Furthermore, tie-lines were drawn between the region referring to C-S-H and other
559 cement hydrates. Several scatter points near portlandite and C-S-H regions were observed in
560 the cured GO-0 and GO-6 samples before acid attack (i.e. red points in Fig. 9). Other than
561 portlandite, the presence of C-S-H was still observed in the sound zone in both samples after
562 attack by citric and sulfuric acids (blue and green points in Fig. 9). The points located in the
563 regions with high alumina, high silica, and low calcium contents in the scatter plot represented
564 the decalcified ettringite, monosulfate and C-S-H. This data suggested that the GO-0 and GO-
565 6 samples experienced a mild decalcifying in the sound zone. However, when compared to
566 GO-0 sample, the number of scatter points corresponding to the decalcified products in the
567 sound zone of GO-6 sample was comparatively smaller. This suggests that the presence of GO
568 in the binder matrix resisted the removal of Ca^{2+} ions from the cement hydrates (e.g. ettringite
569 and C-S-H) into the external solutions.
570



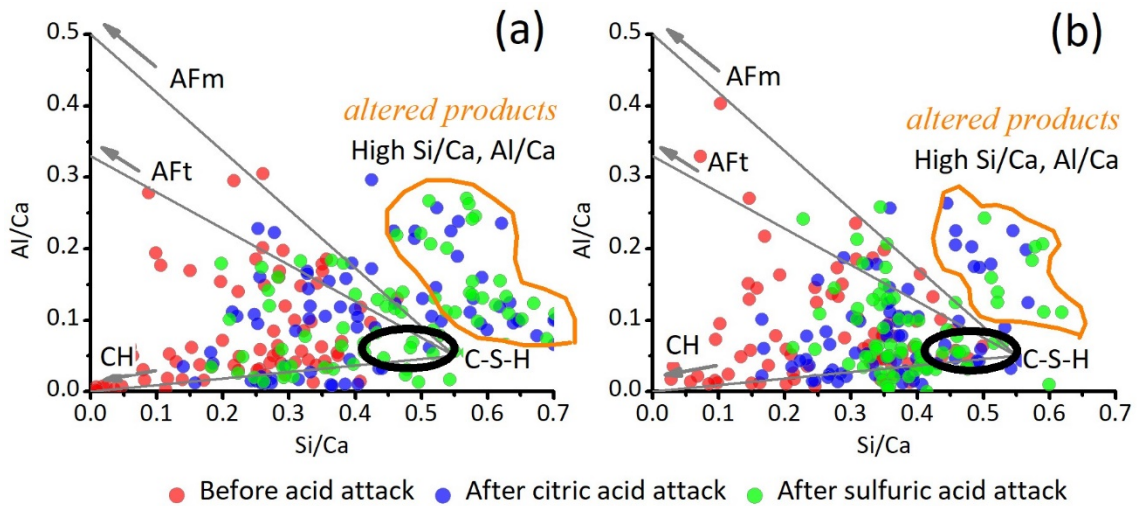
571

572

573 **Fig. 8** SEM-BSE images showing the polished surfaces of GO-0 and GO-6 samples: (a)

574 before acid attack, (b) after citric acid attack, and (c) after sulphuric acid attack

575



576

577

578 **Fig. 9** EDS analyses before and after acid attack of: (a) GO-0 and (b) GO-6 samples (i.e. data
579 collected from the sound zone)

580

581

582 3.6.2. Vickers micro-hardness

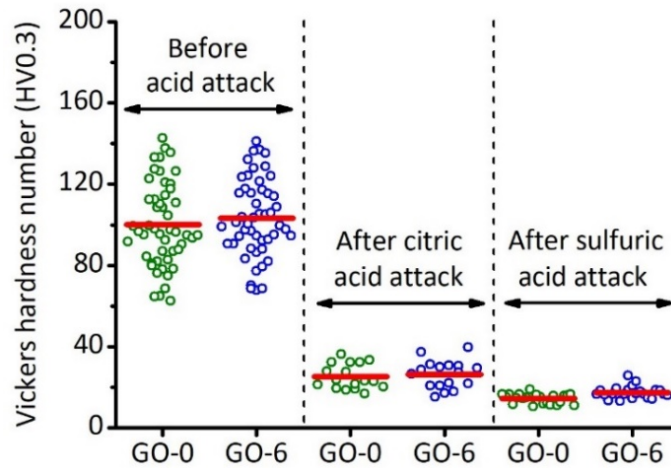
583

584 Fig. 10 provides a comparison of the Vickers hardness number of GO-0 and GO-6 samples (in
585 the altered zone) before and after 14 days of acid exposure. The average hardness number of
586 the binder phase (i.e. omitting the cement particles) in GO-0 and GO-6 samples was 100 and
587 104, respectively. This suggests that the inclusion of 0.09 wt.% GO marginally improved the
588 micro-hardness of cement composites by adequately reinforcing the pores/defective regions in
589 the binder matrix and reducing the growth of micro-cracks. This was in line with the findings
590 of previous studies [58], where the crack reinforcing effect of 1 wt.% GO inclusion was shown
591 to result in improvements in the Young's modulus and fracture stress of a polymeric material
592 (i.e. gelatin) by up to 50% and 60%, respectively. These enhancements were attributed to the
593 presence of GO in the gelatin polymer, which hindered the propagation of micro-cracks and
594 enhanced composite stability.

595

596 The average hardness numbers of the GO-0 and GO-6 samples after citric acid attack (and
597 sulfuric acid attack) were measured as 25 and 27 (and 14 and 17), respectively. The micro-
598 hardness of GO-0 sample decreased by 75% and 86% due to $C_6H_8O_7$ and H_2SO_4 exposures,
599 suggesting that the binder matrix had experienced a severe decalcification. Amongst these,
600 degradation due to H_2SO_4 exposure was found to be relatively higher than degradation due to

601 $C_6H_8O_7$ exposure. The gypsum salt that precipitated in the altered area of H_2SO_4 exposed
 602 samples was relatively softer than the earlandite salt forming in $C_6H_8O_7$ exposed samples.
 603 While the traces of GO remaining in the modified areas might have contributed to the zone
 604 hardness in GO-6 sample, this effect is not expected to be significant, based on the
 605 measurements before acid attack and findings of SEM-EDS analyses presented earlier.
 606



607
 608

609 **Fig. 10** Vickers hardness number of the binder matrix of GO-modified cement samples
 610 before and after acid attack (i.e. data collected from the altered area)

611

612

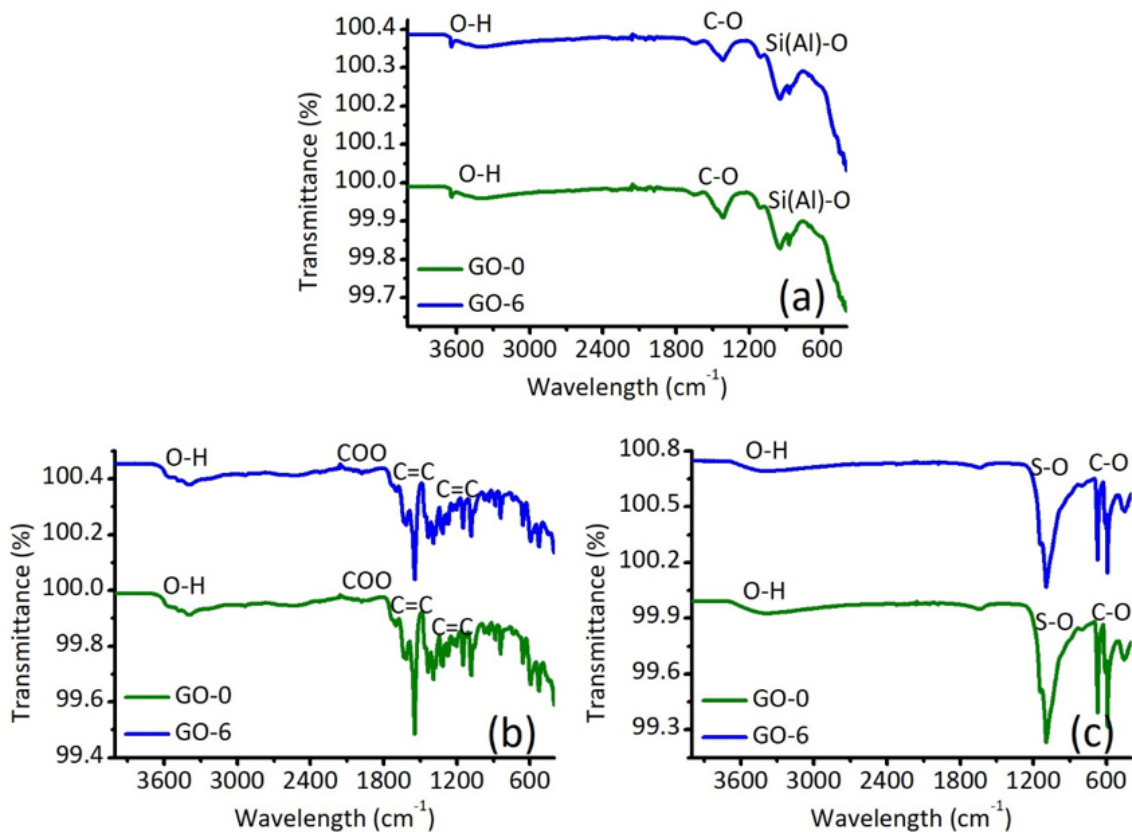
613 3.6.3. FT-IR and XRD

614

615 Figs. 11 and 12 show the FT-IR and XRD results of GO-0 and GO-6 samples (in the altered
 616 zone) before and after 14 days of acid exposure, respectively. The FT-IR bands associated to
 617 Si(Al)-O ($\sim 935\text{ cm}^{-1}$), C-O (1423 cm^{-1}) and O-H (3399 cm^{-1}) functional groups indicated the
 618 formation of C-S-H, calcite, portlandite and free water in the cured samples. These findings
 619 correlated well with the XRD results of GO-0 and GO-6 samples, where the major peaks
 620 confirmed the presence of ettringite ($9.1^\circ 2\theta$), portlandite ($18.1^\circ 2\theta$), calcite ($29.3^\circ 2\theta$),
 621 C_2S/C_3S ($32.2^\circ 2\theta$) and C_4AF ($50.2^\circ 2\theta$) in the pristine cement samples before the acid attack.
 622 A notable reduction in most of these peaks was observed in both samples after $C_6H_8O_7$ and
 623 H_2SO_4 exposures. The similarities in the intensities of the major IR peaks across the two
 624 samples before and after acid attack did not indicate a significant change in the hydration
 625 process via the inclusion of 0.09 wt.% GO.

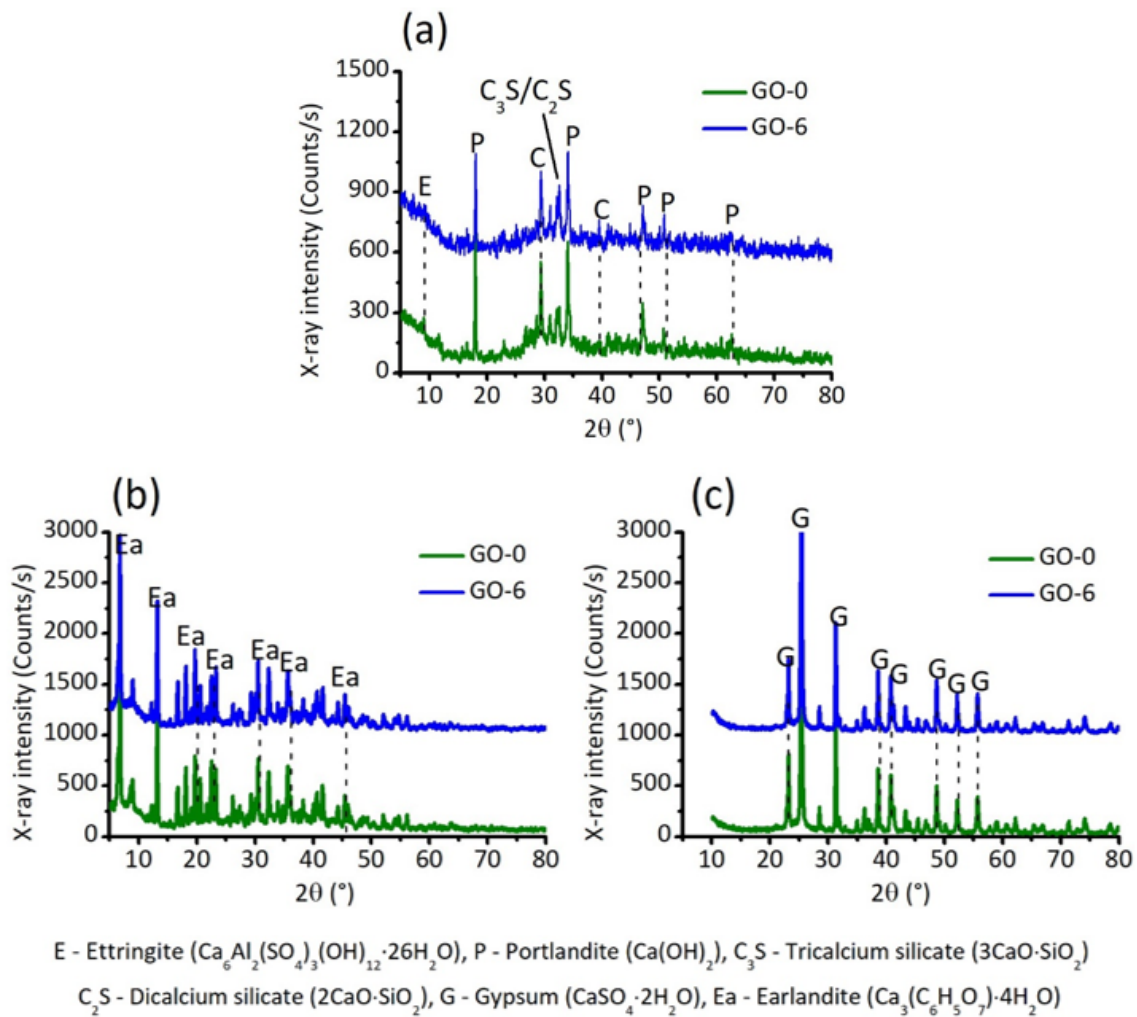
626

627 The FT-IR peaks corresponding to C-C (1259 cm^{-1}), C=C (1542 cm^{-1}) and COO- (1706 cm^{-1})
 628 functional groups suggested the formation of carboxylate salts in the altered zone of GO-0 and
 629 GO-6 samples exposed to $\text{C}_6\text{H}_8\text{O}_7$ solution. Alternatively, the IR peaks corresponding to S-O
 630 (1097 cm^{-1}) functional groups indicated the precipitation of sulfate-bearing salt in these
 631 samples exposed to H_2SO_4 solution. The XRD peaks corresponding to 6.8° , 13.1° , 19.6° , 23.4° ,
 632 30.5° , 35.5° and 45.5° 2θ confirmed the significant precipitation of earlandite
 633 ($\text{Ca}_3(\text{C}_6\text{H}_5\text{O}_7)\cdot 4(\text{H}_2\text{O})$) in the altered areas of both GO-0 and GO-6 samples exposed to $\text{C}_6\text{H}_8\text{O}_7$
 634 solution. In contrast, the formation of gypsum ($\text{CaSO}_4\cdot 2\text{H}_2\text{O}$) was identified in the altered
 635 regions of H_2SO_4 exposed samples via the presence of XRD peaks located at 23° , 25.5° , 31.4° ,
 636 38.8° , 41.1° , 48.8° , 52.2° and 56° 2θ . These observations were in agreement with FT-IR and
 637 SEM findings, where the formation of these salts was noted in the altered zones of both GO-0
 638 and GO-6 samples. Similarly, previous studies [4] reported the formation of earlandite-like (i.e.
 639 calcium citrate tetrahydrate) and gypsum-like (i.e. calcium sulfate dihydrate) salts in the altered
 640 areas of binder matrices exposed to $\text{C}_6\text{H}_8\text{O}_7$ and H_2SO_4 solutions, respectively.
 641



642
 643
 644
 645

Fig. 11 FT-IR spectra of the binder matrix of GO-0 and GO-6 samples in the altered area (a) before acid attack, (b) after citric acid attack, and (c) after sulfuric acid attack



647

648

649 **Fig. 12** XRD patterns of the binder matrix of GO-0 and GO-6 samples in the altered area (a)
 650 before acid attack, (b) after citric acid attack, and (c) after sulfuric acid attack

651

652

653 3.6.4. TGA

654

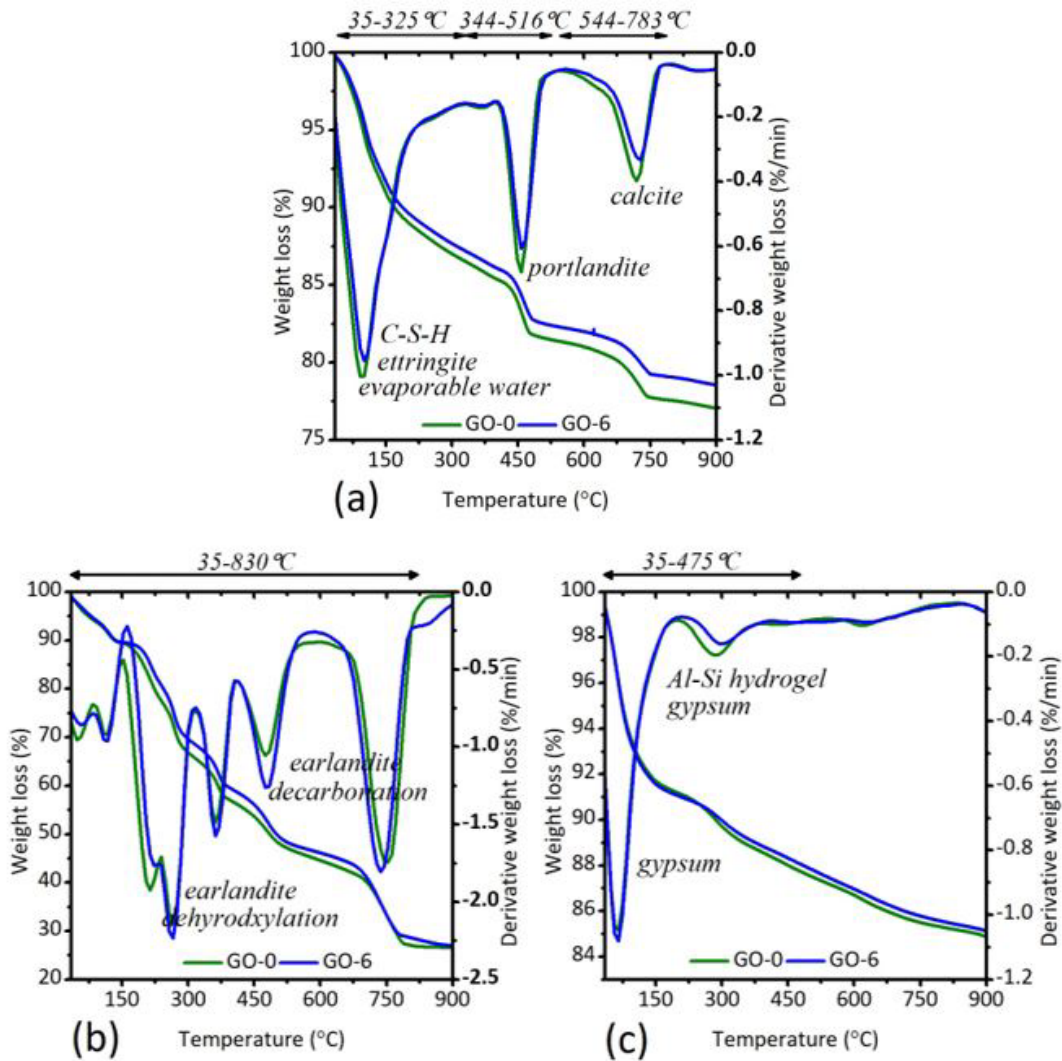
655 Fig. 13 shows the TGA results of GO-0 and GO-6 samples in the altered zone before and after
 656 14 days of acid exposure. The pristine samples before the acid attack revealed a mass loss due
 657 to the evaporation of unbound water, followed by the decomposition of portlandite (405-
 658 508 $^\circ$ C) and calcite (610-783 $^\circ$ C). The analysis of the altered areas of both samples via TGA
 659 revealed findings that agreed with those of XRD and FT-IR. Accordingly, the presence of
 660 ettringite, portlandite, and calcite was not observed in the altered areas of GO-0 and GO-6
 661 samples after $C_6H_8O_7$ and H_2SO_4 exposures. Instead, in line with previous findings, the mass

662 loss due to the thermal decomposition of earlandite (35-827°C) was observed in the altered
663 areas of GO-0 and GO-6 samples at the end of the C₆H₈O₇ attack. Alternatively,
664 dehydroxylation of gypsum and alumina (Al)-silica (Si) hydrogel (219-374°C) was noted in
665 the altered zones of GO-0 and GO-6 samples after H₂SO₄ attack.

666

667 The small amount of GO used in the GO-6 sample was extracted from natural graphite. The
668 combustion of graphite generally starts at 650°C when the dry sample is heated in an ambient
669 environment. Previous studies demonstrated that GO lost 20% of its mass at 200°C under TGA,
670 followed by its decomposition at 550°C [59]. During this process, the first mass loss of GO
671 corresponded to the removal of oxygen-containing functional groups. However, the lower
672 combustion temperature of GO (550°C) in comparison with graphite (650°C) demonstrated the
673 relatively lower thermal stability of GO, which was attributed to the presence of defects created
674 after the elimination of functional oxygen moieties [60]. Accordingly, the mass loss due to GO,
675 albeit very low, might have contributed to the overall mass loss results of GO-6 sample.

676



677

678

679 **Fig. 13** TGA results of the binder matrix in the altered area of GO-0 and GO-6 samples (a)

680 before acid attack, (b) after citric acid attack, and (c) after sulfuric acid attack

681

682 The mass loss observed at each stage was quantified and reported in Table 2 by the procedure
 683 reported in Scrivener et al. [61]. In the samples before acid attack, the mass loss due to bound
 684 water (i.e. present in C-S-H, portlandite, ettringite, and monosulfate) was quantified within the
 685 temperature range of 35-900°C, discounting the mass loss due to carbonation. Accordingly, the
 686 mass loss due to portlandite and calcite in the GO-6 sample was recorded as 14.8% and 6.8%,
 687 which were generally lower than corresponding values presented in the GO-0 sample. These
 688 differences indicated the role the inclusion of 0.09 wt.% GO played in the dissolution of C₃S
 689 and C₃A in the binder matrix and limiting the carbonation process at early ages. The mass loss
 690 corresponding to earlandite in the altered area of GO-6 was slightly lower than that noted in
 691 GO-0 sample. Similar to the trend observed under C₆H₈O₇ attack, the formation of gypsum and

692 Al-Si gel in the altered area of GO-6 was lower than that observed in GO-0 sample (i.e. 11.9%
 693 vs. 12.3%). Correlating with the mass and sectional area loss findings presented earlier, these
 694 values support the overall conclusion on the reinforcement provided by the inclusion of GO,
 695 which increased the resistance of the binder matrix under citric and sulfuric acids.

696

697 **Table 2** Mass loss in the altered zone of GO-0 and GO-6 samples before and after acid
 698 attack, obtained by TGA.

699

Mass loss (%)	Before acid attack		After C ₆ H ₈ O ₇ attack		After H ₂ SO ₄ attack	
	GO-0	GO-6	GO-0	GO-6	GO-0	GO-6
Bound water	19.4	18.4	-	-	-	-
Evaporable water	13	12.4	-	-	-	-
Portlandite	15.6	14.8	-	-	-	-
Calcite	8.2	6.8	-	-	-	-
Earlandite	-	-	73.2	71.9	-	-
Gypsum and Al-Si gel	-	-	-	-	12.3	11.9
Total	23	21.5	73.5	73.1	15.1	14.9

700

701

702 4. CONCLUSIONS

703

704 This study examined the resistance of cement pastes modified by using 0-0.09 wt.% GO
 705 subjected to C₆H₈O₇ and H₂SO₄ environments for two weeks. The GO incorporated in the
 706 prepared mixes was highly oxygenated with an oxygen-to-carbon mass ratio of 0.5. Its edges
 707 and basal plane were effectively grafted with carbonyl, carboxyl, and hydroxyl functional
 708 groups. The inclusion of GO contents beyond 0.03 wt.% led to a retardation in the hydration
 709 of the fresh cement paste, suggesting that higher GO dosages inhibited the hydration of C₃S
 710 and C₃A at early ages. The fresh GO-modified cement pastes showed a shear-thinning
 711 behaviour when the material was sheared up to 100 s⁻¹. An increase in the GO dosage led to a
 712 reduction in the workability of fresh cement pastes, which was associated with the flocculations
 713 enabled by the agglomeration of GO and cement particles at GO contents of > 0.03 wt.%,
 714 providing an enhanced deformation resistance against the shearing force. The agglomeration

715 of GO particles could be evaluated by investigating their dispersion in pore solution as an
716 indication of dispersion in cement mixes, which will be incorporated in future studies.

717

718 The exposure of the prepared samples to $C_6H_8O_7$ and H_2SO_4 environments revealed the
719 formation of an altered zone surrounding the sound zone. Crazeing was more prominent in the
720 altered zones of the H_2SO_4 exposed samples when compared to those exposed to $C_6H_8O_7$.
721 Samples incorporating GO revealed lower losses in terms of mass and sectional area during
722 acid exposure, which improved as the GO content increased. The inclusion of GO led to denser
723 microstructures, thereby limiting the access of aggressive ions from the external solution into
724 the binder matrices. Regardless of the inclusion of GO, the formation of earlandite-like and
725 gypsum-like salts were observed in the binder zone under $C_6H_8O_7$ and H_2SO_4 attacks,
726 respectively. Exposure to $C_6H_8O_7$ and H_2SO_4 environments reduced the micro-hardness of the
727 plain cement pastes, during which the presence of 0.09 wt.% GO enabled slight improvements.
728 The increased resistance of GO-modified samples under acid attack was also verified by
729 microstructural analysis, which enabled the identification of initial hydrate phases and changes
730 in sample composition and microstructure when exposed to the set aggressive environments.

731

732 The findings of this study indicate that GO is one of the potential additives that can modify the
733 microstructure and enhance the service life of concrete against aggressive environments. While
734 these reinforcing benefits of GO were observed for GO contents of up to 0.09%, a balance
735 between the workability and hydration of fresh cement pastes; and durability could be achieved
736 by determining an optimum GO content to be incorporated in cement mixes. Accordingly, an
737 intermediate GO content could not only reduce the deterioration of concrete structures in
738 aggressive environments, but also enable the maintenance of a desired workability and
739 hydration rate for optimum performance in key applications such as chemical warehouses,
740 wastewater sewers and underground tunnels. Considering the potential increase in cost due to
741 the need for surface treatment, the use of GO sheets can be optimized by adjusting their content,
742 resulting in high-performance structural components with a wide range of functionalities.

743

744

745 **ACKNOWLEDGEMENT**

746

747 The authors would like to acknowledge the financial support from the Singapore MOE
748 Academic Research Fund Tier 2 (MOE2017-T2-1-087 (S)) for the completion of this research
749 project.

REFERENCES

- [1] B. Huber, H. Hilbig, M.M. Mago, J.E. Drewes, E. Müller, Comparative analysis of biogenic and chemical sulfuric acid attack on hardened cement paste using laser ablation-ICP-MS, *Cem. Concr. Res.* 87 (2016) 14-21. <https://doi.org/10.1016/j.cemconres.2016.05.003>
- [2] M.G.D. Gutiérrez-Padilla, A. Bielefeldt, S. Ovtchinnikov, M. Hernandez, J. Silverstein, Biogenic sulfuric acid attack on different types of commercially produced concrete sewer pipes, *Cem. Concr. Res.* 40(2) (2010) 293-301. <https://doi.org/10.1016/j.cemconres.2009.10.002>
- [3] A. Bertron, S. Larreur-Cayol, T.T. Le, G. Escadeillas, Degradation of cementitious materials by some organic acids found in agroindustrial effluents, Final Conference of RILEM TC (2009) 96-107.
- [4] M. Alexander, A. Bertron, N. De Belie, Performance of cement-based materials in aggressive aqueous environments, Springer, Netherlands, 2013. <https://doi.org/10.1007/978-94-007-5413-3>
- [5] A. Bertron, J. Duchesne, G. Escadeillas, Degradation of cement pastes by organic acids, *Mater. Struct.* 40(3) (2007) 341-354. <https://doi.org/10.1617/s11527-006-9110-3>
- [6] Y. Yang, T. Ji, X. Lin, C. Chen, Z. Yang, Biogenic sulfuric acid corrosion resistance of new artificial reef concrete, *Constr. Build. Mater.* 158 (2018) 33-41. <https://doi.org/10.1016/j.conbuildmat.2017.10.007>
- [7] T. Wang, K. Wu, L. Kan, M. Wu, Current understanding on microbiologically induced corrosion of concrete in sewer structures: a review of the evaluation methods and mitigation measures, *Constr. Build. Mater.* 247 (2020) 118539. <https://doi.org/10.1016/j.conbuildmat.2020.118539>
- [8] C. Grengg, F. Mittermayr, A. Baldermann, M.E. Böttcher, A. Leis, G. Koraimann, P. Grunert, M. Dietzel, Microbiologically induced concrete corrosion: a case study from a combined sewer network, *Cem. Concr. Res.* 77 (2015) 16-25. <https://doi.org/10.1016/j.cemconres.2015.06.011>
- [9] M. Wu, T. Wang, K. Wu, L. Kan, Microbiologically induced corrosion of concrete in sewer structures: A review of the mechanisms and phenomena, *Constr. Build. Mater.* 239 (2020) 117813. <http://doi.org/10.1016/j.conbuildmat.2019.117813>
- [10] H.A. Khan, A. Castel, M.S.H. Khan, A.H. Mahmood, Durability of calcium aluminate and sulphate resistant Portland cement based mortars in aggressive sewer environment and sulphuric acid, *Cem. Concr. Res.* 124 (2019) 105852. <https://doi.org/10.1016/j.cemconres.2019.105852>
- [11] K.P. Bautista-Gutierrez, A.L. Herrera-May, J.M. Santamaría-López, A. Honorato-Moreno, S.A. Zamora-Castro, Recent progress in nanomaterials for modern concrete infrastructure: advantages and challenges, *Materials* 12(21) (2019) 3548. <https://doi.org/10.3390/ma12213548>
- [12] S. Kawashima, P. Hou, D.J. Corr, S.P. Shah, Modification of cement-based materials with nanoparticles, *Cem. Concr. Compos.* 36 (2013) 8-15. <https://doi.org/10.1016/j.cemconcomp.2012.06.012>
- [13] F. Sanchez, K. Sobolev, Nanotechnology in concrete – a review, *Constr. Build. Mater.* 24(11) (2010) 2060-2071. <https://doi.org/10.1016/j.conbuildmat.2010.03.014>
- [14] M. Muthu, M. Santhanam, Effect of reduced graphene oxide, alumina and silica nanoparticles on the deterioration characteristics of Portland cement paste exposed to acidic environment, *Cem. Concr. Compos.* 91 (2018) 118-137. <https://doi.org/10.1016/j.cemconcomp.2018.05.005>

- [15] M. Murugan, M. Santhanam, S.S. Gupta, T. Pradeep, S.P. Shah, Influence of 2D rGO nanosheets on the properties of OPC paste, *Cem. Concr. Compos.* 70 (2016) 48-59. <https://doi.org/10.1016/j.cemconcomp.2016.03.005>
- [16] H. Yang, L. Jiang, Y. Zhang, Q. Pu, Y. Xu, Predicting the calcium leaching behavior of cement pastes in aggressive environments, *Constr. Build. Mater.* 29 (2012) 88-96. <https://doi.org/10.1016/j.conbuildmat.2011.10.031>
- [17] J.J. Gaitero, I. Campillo, A. Guerrero, Reduction of the calcium leaching rate of cement paste by addition of silica nanoparticles, *Cem. Concr. Res.* 38(8) (2008) 1112-1118. <https://doi.org/10.1016/j.cemconres.2008.03.021>
- [18] J. Gaitero, W. Zhu, I. Campillo, Multi-scale study of calcium leaching in cement pastes with silica nanoparticles, *Nanotechnology in Construction* 3, Springer, 2009, pp. 193-198. <https://doi.org/10.1007/978-3-642-00980-8>
- [19] Z. Lu, A. Hanif, G. Sun, R. Liang, P. Parthasarathy, Z. Li, Highly dispersed graphene oxide electrodeposited carbon fiber reinforced cement-based materials with enhanced mechanical properties, *Cem. Concr. Compos.* 87 (2018) 220-228. <https://doi.org/10.1016/j.cemconcomp.2018.01.006>
- [20] D. Dimov, I. Amit, O. Gorrie, M.D. Barnes, N.J. Townsend, A.I. Neves, F. Withers, S. Russo, M.F. Craciun, Ultrahigh performance nanoengineered graphene–concrete composites for multifunctional applications, *Adv. Funct. Mater.* 28(23) (2018) 1705183. <https://doi.org/10.1002/adfm.201705183>
- [21] X. Li, X. Wang, L. Zhang, S. Lee, H. Dai, Chemically derived, ultrasoft graphene nanoribbon semiconductors, *Sci.* 319(5867) (2008) 1229-1232. <https://doi.org/10.1126/science.1150878>
- [22] Y. Dong, J. Shao, C. Chen, H. Li, R. Wang, Y. Chi, X. Lin, G. Chen, Blue luminescent graphene quantum dots and graphene oxide prepared by tuning the carbonization degree of citric acid, *Carbon* 50(12) (2012) 4738-4743. <https://doi.org/10.1016/j.carbon.2012.06.002>
- [23] M. Muthu, S. Kumar, E.H. Yang, C. Unluer, Degradation of carbonated reactive MgO-based concrete exposed to nitric acid, *J. CO₂ Util.* 36 (2020) 210-219. <https://doi.org/10.1016/j.jcou.2019.11.006>
- [24] L. Zhao, X. Guo, L. Song, Y. Song, G. Dai, J. Liu, An intensive review on the role of graphene oxide in cement-based materials, *Constr. Build. Mater.* 241 (2020) 117939. <https://doi.org/10.1016/j.conbuildmat.2019.117939>
- [25] X. Li, Y.M. Liu, W.G. Li, C.Y. Li, J.G. Sanjayan, W.H. Duan, Z. Li, Effects of graphene oxide agglomerates on workability, hydration, microstructure and compressive strength of cement paste, *Constr. Build. Mater.* 145 (2017) 402-410. <https://doi.org/10.1016/j.conbuildmat.2017.04.058>
- [26] T.S. Qureshi, D.K. Panesar, Impact of graphene oxide and highly reduced graphene oxide on cement based composites, *Constr. Build. Mater.* 206 (2019) 71-83. <https://doi.org/10.1016/j.conbuildmat.2019.01.176>
- [27] D. Li, M.B. Mueller, S. Gilje, R.B. Kaner, G.G. Wallace, Processable aqueous dispersions of graphene nanosheets, *Nat. Nanotechnol.* 3(2) (2008) 101-105. <https://doi.org/10.1038/nnano.2007.451>
- [28] W.S. Hummers, R.E. Offeman, Preparation of graphitic oxide, *J. Am. Chem. Soc.* 80(6) (1958) 1339-1339. <https://doi.org/10.1021/ja01539a017>
- [29] S. Ghazizadeh, P. Duffour, N.T. Skipper, Y. Bai, Understanding the behaviour of graphene oxide in Portland cement paste, *Cem. Concr. Res.* 111 (2018) 169-182. <https://doi.org/10.1016/j.cemconres.2018.05.016>
- [30] Q. Zheng, B. Han, X. Cui, X. Yu, J. Ou, Graphene-engineered cementitious composites: small makes a big impact, *Nanomater. Nanotechnol.* 7 (2017) 18 pages. <https://doi.org/10.1177/1847980417742304>

- [31] B. Han, S. Ding, J. Wang, J. Ou, Nano-engineered cementitious composites: principles and practices, Springer, Singapore, 2019. <https://doi.org/10.1007/978-981-13-7078-6>
- [32] H. Yang, M. Monasterio, H. Cui, N. Han, Experimental study of the effects of graphene oxide on microstructure and properties of cement paste composite, *Compos. Part A Appl. Sci. Manuf.* 102 (2017) 263-272. <https://doi.org/10.1016/j.compositesa.2017.07.022>
- [33] S.K.U. Rehman, Z. Ibrahim, M. Jameel, S.A. Memon, M.F. Javed, M. Aslam, K. Mehmood, S. Nazar, Assessment of rheological and piezoresistive properties of graphene based cement composites, *Int. J. Concr. Struct. Mater.* 12(1) (2018) 64. <https://doi.org/10.1186/s40069-018-0293-0>
- [34] S. Lv, Y. Ma, C. Qiu, Q. Zhou, Regulation of GO on cement hydration crystals and its toughening effect, *Mag. Concr. Res.* 65(20) (2013) 1246-1254. <https://doi.org/10.1680/mac.13.00190>
- [35] W. Jiang, X. Li, Y. Lv, M. Zhou, Z. Liu, Z. Ren, Z. Yu, Cement-based materials containing graphene oxide and polyvinyl alcohol fiber: Mechanical properties, durability, and microstructure, *Nanomaterials* 8(9) (2018) 638. <https://doi.org/10.3390/nano8090638>
- [36] W. Li, X. Li, S.J. Chen, Y.M. Liu, W.H. Duan, S.P. Shah, Effects of graphene oxide on early-age hydration and electrical resistivity of Portland cement paste, *Constr. Build. Mater.* 136 (2017) 506-514. <https://doi.org/10.1016/j.conbuildmat.2017.01.066>
- [37] M. Muthu, N. Ukrainczyk, E. Koenders, Effect of graphene oxide dosage on the deterioration properties of cement pastes exposed to an intense nitric acid environment, *Constr. Build. Mater.* 269 (2021) 121272. <https://doi.org/10.1016/j.conbuildmat.2020.121272>
- [38] SS EN 197-1, Cement (Part 1): composition, specifications and conformity criteria for common cement, Singapore Standards Council, SPRING Singapore (2014) 46 pages. <https://www.nlb.gov.sg/biblio/201398199>
- [39] ASTM C1702, Standard test method for measurement of heat of hydration of hydraulic cementitious materials using isothermal conduction calorimetry, ASTM International, Pennsylvania, USA (2009) 9 pages. <https://doi.org/10.1520/C1702-09A>
- [40] M. Muthu, E.-H. Yang, C. Unluer, Resistance of graphene oxide-modified cement pastes to hydrochloric acid attack, *Constr. Build. Mater.* 273 (2021) 121990. <https://doi.org/10.1016/j.conbuildmat.2020.121990>
- [41] ASTM E384, Standard test method for microindentation hardness of materials, ASTM International, Pennsylvania, USA (2017) 40 pages. <https://doi.org/10.1520/E0384-17>
- [42] Y. Dang, X. Shi, J. Qian, Y. Jiang, X. Li, Statistical Characteristics of Microhardness of Hardened Cement Paste, *Journal of Wuhan University of Technology-Mater. Sci. Ed.* 33(4) (2018) 924-931. <https://doi.org/10.1007/s11595-018-1914-9>
- [43] D.C. Marcano, D.V. Kosynkin, J.M. Berlin, A. Sinitskii, Z. Sun, A. Slesarev, L.B. Alemany, W. Lu, J.M. Tour, Improved synthesis of graphene oxide, *ACS Nano* 4(8) (2010) 4806-4814. <https://doi.org/10.1021/nn1006368>
- [44] G. Xu, S. Du, J. He, X. Shi, The role of admixed graphene oxide in a cement hydration system, *Carbon* 148 (2019) 141-150. <https://doi.org/10.1016/j.carbon.2019.03.072>
- [45] Z. Lu, X. Li, A. Hanif, B. Chen, P. Parthasarathy, J. Yu, Z. Li, Early-age interaction mechanism between the graphene oxide and cement hydrates, *Constr. Build. Mater.* 152 (2017) 232-239. <https://doi.org/10.1016/j.conbuildmat.2017.06.176>
- [46] X. Sun, Q. Wu, J. Zhang, Y. Qing, Y. Wu, S. Lee, Rheology, curing temperature and mechanical performance of oil well cement: Combined effect of cellulose nanofibers and graphene nano-platelets, *Mater. Des.* 114 (2017) 92-101. <https://doi.org/10.1016/j.matdes.2016.10.050>
- [47] F. Irgens, *Rheology and non-newtonian fluids*, Springer, 2014. <https://doi.org/10.1007/978-3-319-01053-3>

- [48] T. Gutberlet, H. Hilbig, R.E. Beddoe, Acid attack on hydrated cement - effect of mineral acids on the degradation process, *Cem. Concr. Res.* 74 (2015) 35-43. <https://doi.org/10.1016/j.cemconres.2015.03.011>
- [49] A. Bertron, Understanding interactions between cementitious materials and microorganisms: a key to sustainable and safe concrete structures in various contexts, *Mater. Struct.* 47(11) (2014) 1787-1806. <https://doi.org/10.1617/s11527-014-0462-9>.
- [50] G.W. Scherer, Theory of drying, *J. Am. Ceram. Soc.* 73(1) (1990) 3-14. <https://doi:10.1111/j.1151-2916.1990.tb05082.x>
- [51] J.J. Chen, J.J. Thomas, H.M. Jennings, Decalcification shrinkage of cement paste, *Cem. Concr. Res.* 36(5) (2006) 801-809. <https://doi.org/10.1016/j.cemconres.2005.11.003>
- [52] W.-J. Long, T.H. Ye, Y.-C. Gu, H.-D. Li, F. Xing, Inhibited effect of graphene oxide on calcium leaching of cement pastes, *Constr. Build. Mater.* 202 (2019) 177-188. <https://doi.org/10.1016/j.conbuildmat.2018.12.194>
- [53] A. Peyvandi, P. Soroushian, A.M. Balachandra, K. Sobolev, Enhancement of the durability characteristics of concrete nanocomposite pipes with modified graphite nanoplatelets, *Constr. Build. Mater.* 47 (2013) 111-117. <https://doi.org/10.1016/j.conbuildmat.2013.05.002>
- [54] A. Peyvandi, P. Soroushian, N. Abdol, A.M. Balachandra, Surface-modified graphite nanomaterials for improved reinforcement efficiency in cementitious paste, *Carbon* 63 (2013) 175-186. <https://doi.org/10.1016/j.carbon.2013.06.069>
- [55] K. Gong, Z. Pan, A.H. Korayem, L. Qiu, D. Li, F. Collins, C.M. Wang, W.H. Duan, Reinforcing effects of graphene oxide on portland cement paste, *J. Mater. Civil. Eng.* 27(2) (2014) A4014010. [https://doi.org/10.1061/\(ASCE\)MT.1943-5533.0001125](https://doi.org/10.1061/(ASCE)MT.1943-5533.0001125)
- [56] D. Hou, T. Yang, J. Tang, S. Li, Reactive force-field molecular dynamics study on graphene oxide reinforced cement composite: functional group de-protonation, interfacial bonding and strengthening mechanism, *Phys. Chem. Chem. Phys.* 20(13) (2018) 8773-8789. <https://doi.org/10.1039/C8CP00006A>
- [57] W. Meng, K.H. Khayat, Effect of graphite nanoplatelets and carbon nanofibers on rheology, hydration, shrinkage, mechanical properties, and microstructure of UHPC, *Cem. Concr. Res.* 105 (2018) 64-71. <https://doi.org/10.1016/j.cemconres.2018.01.001>
- [58] S. Panzavolta, B. Bracci, C. Gualandi, M.L. Focarete, E. Treossi, K. Kouroupis-Agalou, K. Rubini, F. Bosia, L. Brely, N.M. Pugno, V. Palermo, A. Bigi, Structural reinforcement and failure analysis in composite nanofibers of graphene oxide and gelatin, *Carbon* 78 (2014) 566-577. <https://doi.org/10.1016/j.carbon.2014.07.040>
- [59] V. Georgakilas, *Functionalization of graphene*, John Wiley & Sons, Hoboken, USA, 2014. <https://doi.org/10.1002/9783527672790>
- [60] G. Wang, J. Yang, J. Park, X. Gou, B. Wang, H. Liu, J. Yao, Facile synthesis and characterization of graphene nanosheets, *J. Phys. Chem.* 112(22) (2008) 8192-8195. <https://doi.org/10.1021/jp710931h>
- [61] K. Scrivener, R. Snellings, B. Lothenbach, *A practical guide to microstructural analysis of cementitious materials*, Taylor & Francis Group, Boca Raton, USA, 2016. <https://doi.org/10.1201/b19074>